

**Lattice dynamics and phonon dispersion of van der Waals layered
ferromagnet Fe₃GaTe₂**

Xia Chen,^a Xi Zhang,^a Wenjie He,^a Yu Li,^b Jiating Lu,^c Dinghua Yang,^a Deren Li,^a Li Lei,^b

Yong Peng^d and Gang Xiang^{*a}

^a College of Physics, Sichuan University, Chengdu 610064, China

^b Institute of Atomic and Molecular Physics, Sichuan University, Chengdu 610064, China

^c College of Information and Engineering, Sichuan Tourism University, Chengdu 610064, China

^d School of Materials and Energy, Lanzhou University 730000, China

***Corresponding authors' email:** gxiang@scu.edu.cn (G.X.)

Abstract

Van der Waals (vdW) layered ferromagnet Fe_3GaTe_2 shows great potential in two-dimensional spintronic application due to its robust room-temperature ferromagnetism and large perpendicular magnetic anisotropy. Despite the tremendous progress in the spintronic and electronic studies of Fe_3GaTe_2 , much less effort has been spent on the understanding of lattice dynamics and its possible interaction with spintronic and electronic degrees of freedom in Fe_3GaTe_2 . In this work, by combining Raman spectroscopic data in a wide range of pressure (atmospheric pressure~19.5 GPa) and temperature (80 K~690 K) with first-principles calculation results, we systematically studied the lattice dynamics and phonon dispersion of Fe_3GaTe_2 . Our results show that the phonon energies of Fe_3GaTe_2 located at 126.0 cm^{-1} and 143.5 cm^{-1} originate from the E_{2g}^2 and A_{1g}^1 vibration modes, respectively, and the nature of the E_{2g}^2 mode is anharmonic while that of the A_{1g}^1 mode is quasi-harmonic. Furthermore, the spin-phonon coupling in Fe_3GaTe_2 is discovered by identifying the anomalies in the Raman data right below the Curie temperature of 360 K, in which the phonon energies and the full widths at half maximum of the E_{2g}^2 mode clearly deviate from the classical anharmonic model. Our findings are valuable for fundamental studies and potential applications of vdW Fe_3GaTe_2 -based materials and devices under variable temperature and pressure conditions.

Introduction

Lattice dynamics is essential for fundamental studies and practical applications of ferromagnetic materials, since the interplay among lattice, charge and spin dynamics significantly influence their intriguing physical properties [1-3]. Very recently, van der Waals (vdW) layered ferromagnet Fe_3GaTe_2 has gained extensive attention for its great potential in information storage applications due to its high Curie temperature (T_c), large spin polarization and strong perpendicular magnetic anisotropy [4-8]. However, although great progress has been achieved in the spintronic and electronic studies of Fe_3GaTe_2 [9-11], much less effort has been spent on the understanding of lattice dynamics and its possible interaction with spintronic and electronic degrees of freedom in Fe_3GaTe_2 . Despite a few studies on the Raman spectroscopy of Fe_3GaTe_2 [5,12], the lattice dynamics of Fe_3GaTe_2 is still ambiguous and the assignment of vibrational modes, especially the E_{2g}^2 and A_{1g}^1 modes, has been based more on intuition than reasoning. As is known, Raman spectroscopy under high pressure up to tens of GPa and high temperature above the T_c can be used to explore the atomic-level interactions and advance the understanding of the interplay among lattice vibrations, charge carriers and spin excitations in solid-state materials [13-21]. However, no systematic studies on pressure- and temperature-dependent lattice dynamics of Fe_3GaTe_2 have been investigated yet.

In this work, we investigate lattice dynamics and phonon dispersion of Fe_3GaTe_2 through Raman spectroscopic measurements under a wide range of pressure (atmospheric pressure \sim 19.5 GPa) and temperature (80 K \sim 690 K) in collaboration with first-principles calculations. Based on theoretical calculation of phonon energies and experimental observation of lattice modes through pressure-dependent Raman measurements, two Raman peaks located at 126.0 cm^{-1} and 143.5 cm^{-1} are identified as the E_{2g}^2 and A_{1g}^1 vibration modes, respectively, which is different from previously-reported results [5,12]. Interestingly, under high pressure, the E_{2g}^2 mode softens and the A_{1g}^1 mode slightly stiffens, indicating the nature of the E_{2g}^2 mode is anharmonic and that of the A_{1g}^1 is quasi-harmonic. Furthermore, the temperature-dependent Raman data reveals the signature of spin-phonon coupling in Fe_3GaTe_2 , where the phonon energy and the FWHM of the E_{2g}^2 mode deviate from anharmonic model as the

temperature decreases below the T_c of 360 K.

Results and Discussion

The microstructural and magnetic properties of bulk Fe_3GaTe_2 are first characterized. VdW layered ferromagnet Fe_3GaTe_2 composed of Te/ Fe_3Ga /Te layers exhibits a hexagonal crystal structure, as shown in Fig. 1(a), belonging to $P6_3/mmc$ (No. 194) space group and D_{6h}^4 ($6/mmm$) point group. Atomic force microscopy (AFM) image in Fig. 1(b) indicates that the studied Fe_3GaTe_2 is as thick as ~ 127 nm. Figs. 1(c) and 1(d) present the high-resolution high-angle annular dark-field scanning transmission electron microscopy (HAADF-STEM) images along the [100] and [001] orientations, revealing that the lattice constants a and c are 4.12 ± 0.03 Å and 16.27 ± 0.05 Å, respectively. Fig. 1(e) shows the energy-dispersive X-ray spectroscopy (EDS) mapping of Fe, Ga and Te atoms, where the nicely arranged atomic distributions underscore high quality of the layered structure of Fe_3GaTe_2 . For details regarding the XRD pattern of bulk Fe_3GaTe_2 , one can refer to our prior work [22]. The surface composition and chemical states of Fe_3GaTe_2 are characterized by X-ray photoelectron spectroscopy (XPS) of Fe $2p$, Ga $2p$ and Te $3d$ core levels. Fig. 1(f) illustrates the decomposed Fe $2p$ spectrum, where the $2p_{1/2}$ and $2p_{3/2}$ peaks at 720.0 eV and 706.9 eV correspond to the Fe^0 state and the peaks at 724.1 eV and 710.5 eV correspond to the Fe^{3+} state, accompanied by the satellite peaks at 727.4 eV and 714.7 eV [6]. Fig. 1(g) shows the peaks at 1144.4 eV and 1117.6 eV, which are identified as Ga $2p_{1/2}$ and $2p_{3/2}$, respectively [6]. Fig. 1(h) illustrates the prominent peaks at 582.7 eV and 572.3 eV, which are identified as Te $3d_{3/2}$ and Te $3d_{5/2}$, respectively, and indicate the existence of Te^{2-} [6,23], and the weak peaks at 587.4 eV and 574.1 eV indicate the existence of Te^{4+} due to oxidization [23]. The magnetic properties of bulk Fe_3GaTe_2 are examined by superconducting quantum interference device (SQUID) and shown in Figs. 1(i)-1(l). Fig. 1(i) illustrates the temperature-dependent magnetization curves, indicating that the saturation magnetization (M_s) rises from 22.5 emu/g to 54.7 emu/g and the coercivity (H_c) increases from 76.6 Oe to 264.2 Oe as the temperature drops from 350 K to 2 K (Fig. 1j). Fig. 1(k) shows that the bulk Fe_3GaTe_2 exhibits superior M_s under out-of-plane magnetic field at 300 K, revealing its strong perpendicular magnetic anisotropy at room temperature. The field-cooling magnetization curve in Fig. 1(l)

reveals that the T_c of bulk Fe_3GaTe_2 is ~ 360 K, well above room temperature.

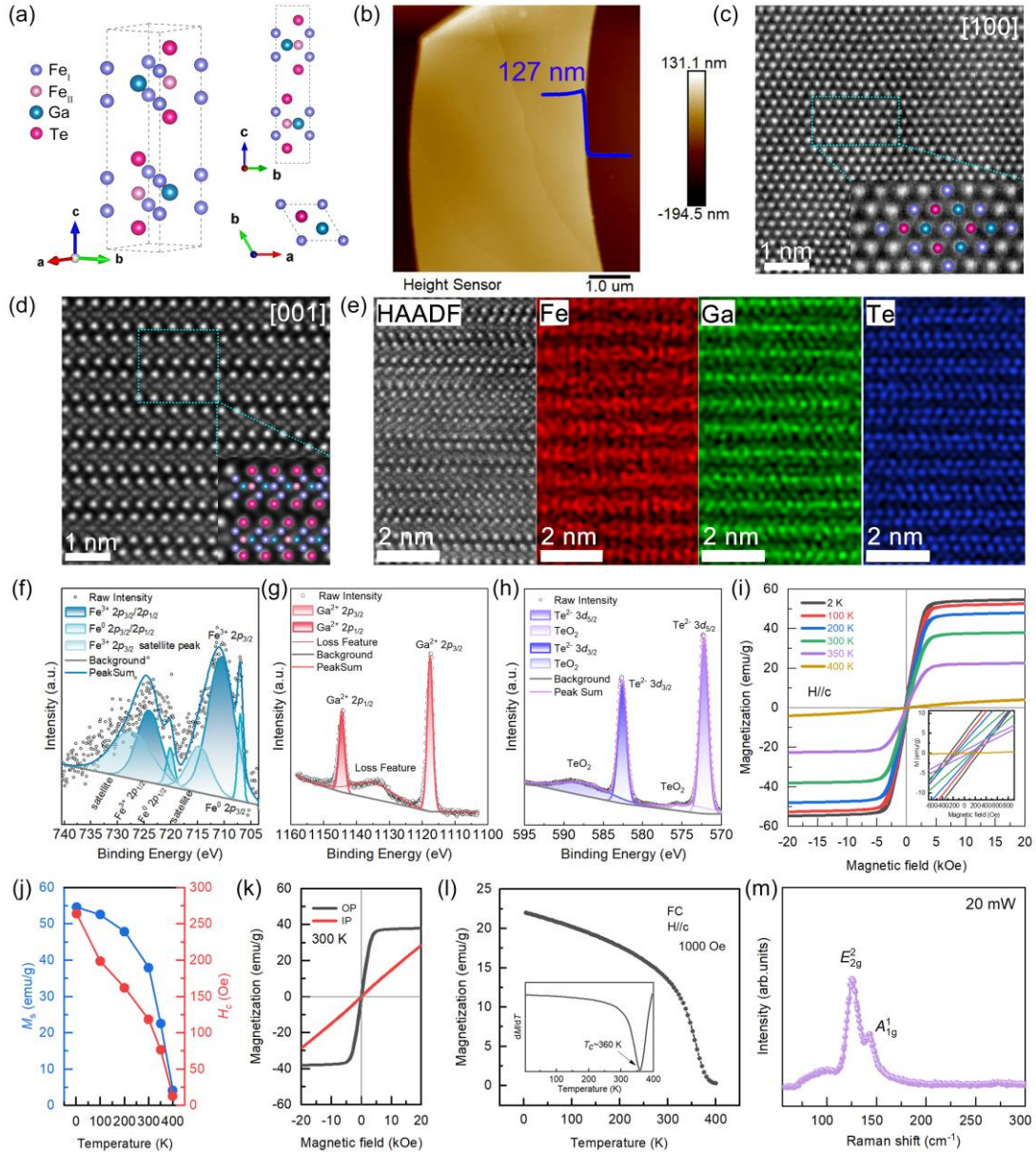


Fig. 1. (a) Crystal structure of bulk Fe_3GaTe_2 . (b) AFM image of the 127 nm-thick Fe_3GaTe_2 flake. The HAADF-STEM images viewed along the (c) [100] and (d) [001] orientations of the Fe_3GaTe_2 flake, where the insets show the magnified atomic structures. (e) STEM-EDS elemental mapping of the Fe_3GaTe_2 flake along the [001] orientation. XPS of the fresh Fe_3GaTe_2 flake for the (f) Fe, (g) Ga and (h) Te elements. (i) Magnetic field-dependent magnetization curves of bulk Fe_3GaTe_2 at various temperatures. The inset shows magnified curves around zero field. (j) Temperature-dependent saturation magnetization and coercivities for bulk Fe_3GaTe_2 . (k) In-plane and out-of-plane magnetization curves of bulk Fe_3GaTe_2 at 300 K. (l) Out-of-plane field cooling magnetization curve of Fe_3GaTe_2 . The inset presents the temperature-dependent dM/dT , indicating that the T_c is ~ 360 K. (m) Raman spectroscopy of Fe_3GaTe_2 flake.

According to space group theory, Fe_3GaTe_2 owns an irreducible representation of $\Gamma=4A_{2u}+4E_{1u}+4E_{2g}+4B_{2g}+2A_{1g}+2E_{2u}+2E_{1g}+2B_{1u}$ at the center of the Brillouin zone, where the E_{1g} and E_{2g} modes are doubly degenerate and the A_{1g} and E_{2g} modes are Raman-active phonons, the same as its isostructural counterpart Fe_3GeTe_2 [24-26]. At 20 mW excitation power, two phonon energies located at 126.0 cm^{-1} and 143.5 cm^{-1} are measured in the Fe_3GaTe_2 flake, as shown in Fig. 1(m). The first-principles calculations are employed to identify the vibrational modes, as shown in Table I, where the calculated phonon energies of 118.7 cm^{-1} and 142.7 cm^{-1} are assigned to the E_{2g}^2 and A_{1g}^1 modes, respectively, corresponding to the measured values of 126.0 cm^{-1} and 143.5 cm^{-1} . The small discrepancy between the calculated and measured phonon energies is due to the harmonic approximation used in VASP for phonon energy calculation [27].

Table I. Calculated and experimental values of phonon energies in bulk Fe_3GaTe_2

Symmetry	Calculated (cm^{-1})				Experimental
	FM ground state		AFM ground state		300 K
	D2	D3	Optb86b	Optb86b	
E_{2g}^1	23.4	17.9	16.2	20.5	-
E_{1g}^1	71.4	68.7	68.3	70.3	-
E_{2g}^2	118.7	117.4	117.1	119.9	126.0
A_{1g}^1	142.7	144.3	141.1	139.8	143.5
E_{1g}^2	206.7	210.7	210.4	209.6	-
E_{2g}^3	222.5	228.0	228.4	232.1	-
A_{1g}^2	256.2	264.9	268.1	264.9	-
E_{2g}^4	328.5	323.6	325.3	326.5	-

The assignment of vibrational modes is further verified by pressure-dependent Raman spectroscopic measurements. The schematic of the measurement setup and the Raman data under various pressures are shown in Figs. 2(a)-2(c). Notably, the contour-color map of pressure-dependent Raman intensity in Fig. 2(d) reveals that the E_{2g}^2 mode at 126.7 cm^{-1} exhibits much higher intensity than the A_{1g}^1 mode at 143.8 cm^{-1} does, indicating the microstructural integrity of the Fe_3GaTe_2 placed onto the diamond anvil cells (DAC). Fitted

by a Gauss+Lor function, the phonon energy of the E_{2g}^2 mode monotonically decreases from 126.7 cm^{-1} to 101.8 cm^{-1} as the pressure increases from ambient to 10.8 GPa, and then stabilizes, as shown in Fig. 2(e). Conversely, the phonon energy of the A_{1g}^1 mode exhibits an overall blue-shift: it initially increases from 143.8 cm^{-1} to 145.9 cm^{-1} as the pressure increases from ambient pressure to 5.7 GPa, and finally increases to 146.5 cm^{-1} at 19.5 GPa, as shown in Fig. 2(f). Meanwhile, the full widths at half maximum (FWHMs) of the E_{2g}^2 and A_{1g}^1 modes broaden significantly with increasing pressure, indicating higher phonon scattering and reduced phonon lifetime. Upon releasing pressure, the re-emergence of sharp Raman peak as well as a slight redshift (2 cm^{-1}) in the phonon energy of the E_{2g}^2 mode under $\sim 0 \text{ GPa}$, as shown in Figs. 2(c) and 2(g), indicate that the Fe_3GaTe_2 , with gentle responsiveness to external pressure, is suitable for the vdW-based flexible sensors [28].

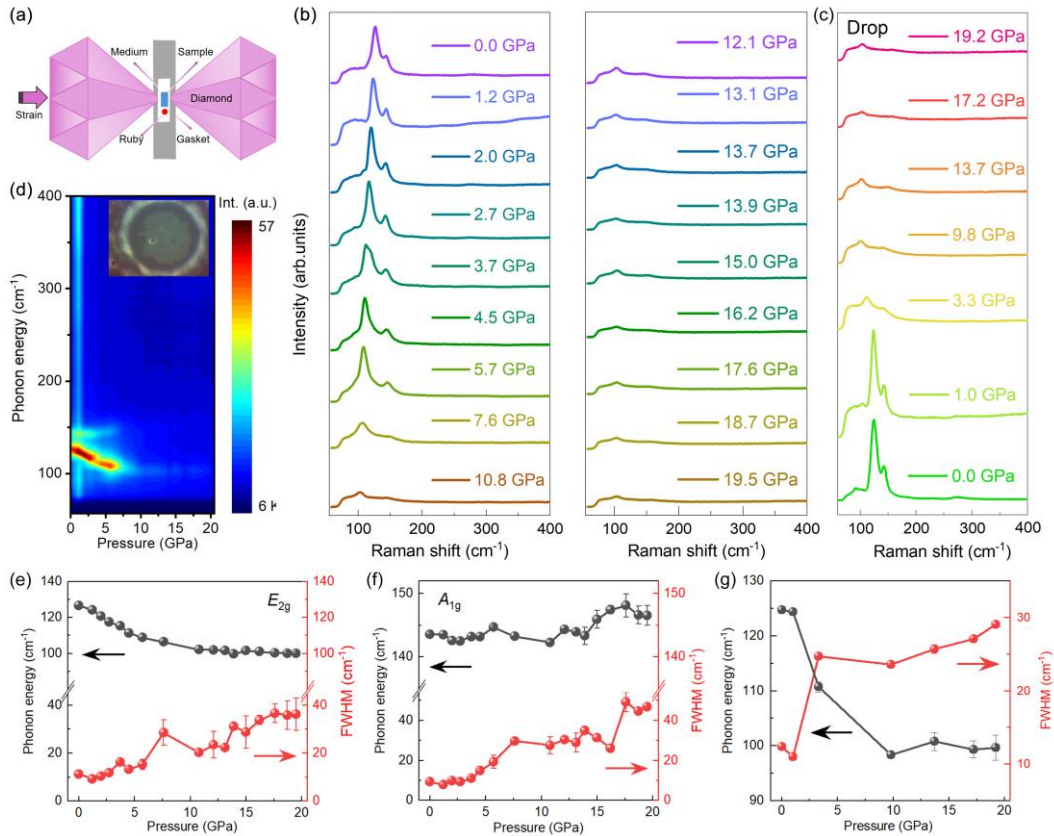


Fig. 2. *In-situ* high-pressure Raman spectroscopic measurements of Fe_3GaTe_2 using DAC. (a) A schematic diagram of DAC. (b) Raman spectroscopies upon applying pressure ranging from 0.0 GPa to 19.5 GPa. (c) Releasing pressure-dependent Raman spectroscopies. (d) Pressures-dependent Raman intensities at 300 K.

The inset shows the microphotograph of the Fe_3GaTe_2 within DAC. Pressure-dependent phonon energies and FWHMs of the (e) E_{2g}^2 and (f) A_{1g}^1 modes. (g) Releasing pressure-dependent phonon energies and FWHMs for the E_{2g}^2 mode.

Then the vibrational nature of the E_{2g} and A_{1g} modes are studied by combining first-principles calculation results and experimental data. The atomic displacement patterns of the E_{2g} and A_{1g} modes in bulk Fe_3GaTe_2 with ferromagnetic state presented in Fig. 3(a) show that the E_{2g}^2 mode features Te and Fe/Ga atoms vibrating in opposite directions within ab -plane, whereas the A_{1g}^1 mode involves the Te and Fe_I atoms vibrating in the c -plane. Moreover, the phonon dispersion in Figs. 3(b) and S1(a)-(f) (see Supplemental Material) shows that all frequencies within the Brillouin zone are real, indicating no structural phase transition under high pressure. Meanwhile, the contributions of Fe, Ga and Te atoms to different frequencies are also visualized, where the frequencies below 150 cm^{-1} mainly arise from the Te/Ga atoms and partially stem from the Fe atoms, while higher frequencies are primarily from the Fe atoms, with small contributions from the Te/Ga atoms. Fig. 3(c) reveals that the lattice constant c and volume decrease significantly with increasing pressure, which likely strengthens interlayer interactions and contributes to the hardening of the A_{1g}^1 mode associated with out-of-plane vibrations, as explained by the quasi-harmonic approximation [29]. By combining X-ray diffraction patterns under high pressure [30] with the calculated pressure-dependent volume in our work, it is found that the value of bulk modulus $K = -V \frac{dP}{dV}$ in Fe_3GaTe_2 is positive, where V and P represent volume and pressure, respectively. According to the isothermal model, Grüneisen parameter is given by $\gamma_{iT} = -\left(\frac{d \ln(\omega_i)}{d \ln(V_i)}\right)_T = \frac{K}{\omega_i} \left(\frac{d\omega_i}{dP}\right)_T$, where P is pressure and ω_i is the phonon energy of the i -th phonon mode [29, 31]. The analysis of the pressure-dependent phonon energy (Fig. 2d) suggests that the value of γ_{iT} for the E_{2g}^2 mode in Fe_3GaTe_2 is negative, indicating its anharmonicity, similar to that in Fe_3GeTe_2 [29]. It is worthwhile noting that the calculated phonon energies of the E_{2g}^2 and A_{1g}^1 modes under high pressure shown in Fig. 3(d) are well consistent with the experimental

results, as evidenced by the softening of the E_{2g}^2 mode and the hardening of the A_{1g}^1 mode with increasing pressure.

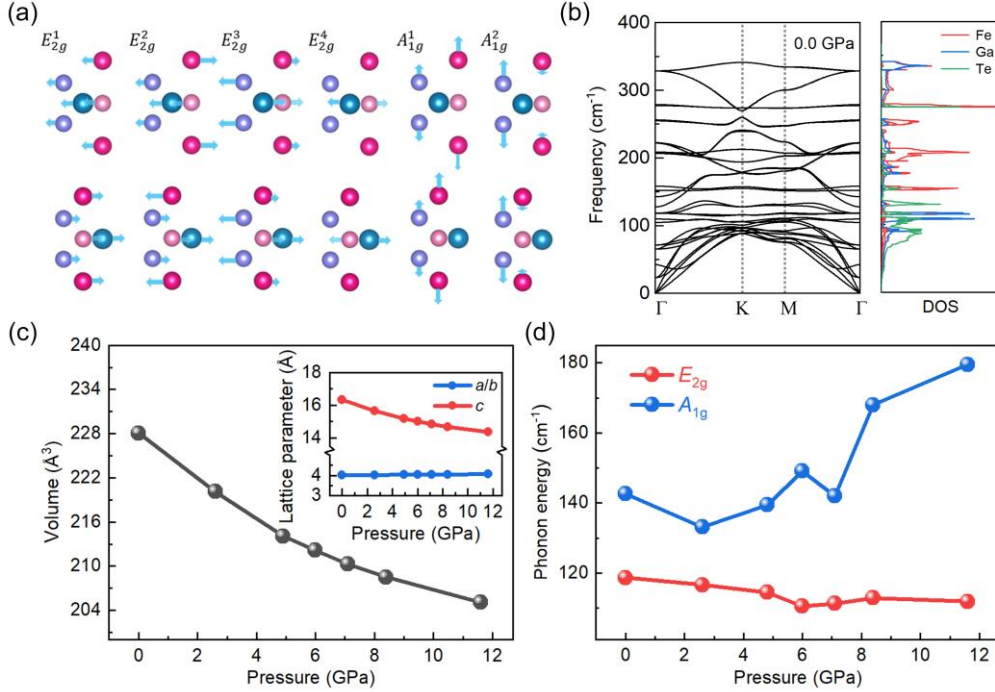


Fig. 3. (a) Atomic displacement patterns of the bulk Fe_3GaTe_2 with ferromagnetic interlayer interaction, where the bright pink, blue, and purple (or pale pink) atoms represent the Te, Ga and Fe atoms, respectively, and the arrows (arrows lengths) represent the vibrational direction (vibrational strength). (b) Calculated phonon dispersion and projected phonon density of states (PDOS) of bulk Fe_3GaTe_2 under ambient pressure. (c) Calculated pressure-dependent volume of bulk Fe_3GaTe_2 , where the inset shows the lattice parameters as a function of pressure. (d) Calculated pressure-dependent phonon energies for the E_{2g}^2 (red ball) and A_{1g}^1 modes (blue ball).

Finally, we discuss the possible spin-phonon coupling in Fe_3GaTe_2 through temperature-dependent phonon energies and FWHMs of the E_{2g}^2 and A_{1g}^1 modes. The temperature-dependent Raman spectroscopic data of the Fe_3GaTe_2 are shown in Fig. 4(a). The phonon energies of the E_{2g}^2 and A_{1g}^1 modes exhibit blueshift as the temperature decreases, where the E_{2g}^2 (A_{1g}^1) mode increases from 121.6 (140.2) cm^{-1} at 540 K to 126.0 cm^{-1} (143.5) at 300 K, and further to 129.0 (146.5) cm^{-1} at 80 K, as shown in Figs. 4(b) and 4(c). Interestingly, the phonon energy of the E_{2g}^2 mode is hardened through decreasing the temperature, different from the fact that the E_{2g}^2 phonon energy is softened through increasing the

pressure. These behaviors in Fe_3GaTe_2 are similar to those observed in Fe_3GeTe_2 [29], which could be explained by the variable magnetic ordering due to the changes of magnetic exchange interactions influenced by pressure and temperature [29, 30, 32]. Under high pressure, the competition between intra- and inter-layer exchange interactions and the modifiable density of states near the Fermi level tends to favor the the spin ordering from out-of-plane to in-plane [30], thereby contributing to the softening of the E_{2g}^2 mode (Fig. 2d). In contrast, the spin ordering could be well-arranged along the out-of-plane with decreasing temperature due to suppressed thermal effects, leading to the hardening of the E_{2g}^2 mode (Fig. 4b). The fitting results of the phonon energies and FWHMs for the E_{2g}^2 and A_{1g}^1 modes in Figs. 4(b)-4(e) follow a phonon anharmonic processes model [33]

$$\omega_{anh}(T) = \omega_0 + A \left[1 + \frac{2}{e^{\frac{\hbar\omega_0}{2k_B T}} - 1} \right] + B \left[1 + \frac{3}{e^{\frac{\hbar\omega_0}{3k_B T}} - 1} + \frac{3}{\left(e^{\frac{\hbar\omega_0}{3k_B T}} - 1 \right)^2} \right] \quad (1)$$

$$\Gamma_{anh}(T) = \Gamma_0 + C \left[1 + \frac{2}{e^{\frac{\hbar\omega_0}{2k_B T}} - 1} \right] + D \left[1 + \frac{3}{e^{\frac{\hbar\omega_0}{3k_B T}} - 1} + \frac{3}{\left(e^{\frac{\hbar\omega_0}{3k_B T}} - 1 \right)^2} \right] \quad (2)$$

where the ω_{anh} , ω_0 , Γ_{anh} , Γ_0 , $A(B/C/D)$, \hbar , and k_B represent modulated phonon energy, phonon energy at 0 K, modulated linewidth, linewidth at 0 K, anharmonic constant, Plank's constant and Boltzmann's constant, respectively. In magnetic materials, the temperature-dependent phonon energies can be described by $\omega(T) \propto \omega(0) + \Delta\omega_{latt} + \Delta\omega_{anh} + \Delta\omega_{sp-ph}$, proposed by Granado [34]. Here, the $\omega(0)$ represents the phonon energy at 0 K, and the $\Delta\omega_{latt}$, $\Delta\omega_{anh}$ and $\Delta\omega_{sp-ph}$ correspond to the contributions from the thermal-dependent volume, intrinsic anharmonic effects and the spin-phonon coupling, respectively [34]. Based on this model, both phonon energy and FWHM of the E_{2g}^2 mode well obey an anharmonic model above the T_c of 360 K, confirming the anharmonicity of the E_{2g}^2 mode. Nevertheless, it deviates from the expected anharmonic trend below the T_c , revealing the presence of spin-phonon coupling in Fe_3GaTe_2 , as seen in other materials [27, 35]. For the A_{1g}^1 mode, a similar temperature-dependent behavior is observed in phonon energy, although the FWHM fits well

with the anharmonic model throughout the entire temperature range. This suggests that the deviation of phonon energy in the A_{1g}^1 mode most likely stems from the quasi-harmonic effect and spin-phonon coupling, as seen in YCrO_3 [36]. Last but not least, we should point out that the Fe_3GaTe_2 flake remains stable throughout the whole process of varying pressure and temperature. In fact, the stability of the 2D Fe_3GaTe_2 flake can be distinguished by excitation power-dependent Raman spectroscopic measurements, as shown in Fig. S2 (see Supplemental Material), which provides a fast way for assessing the Fe_3GaTe_2 quality.

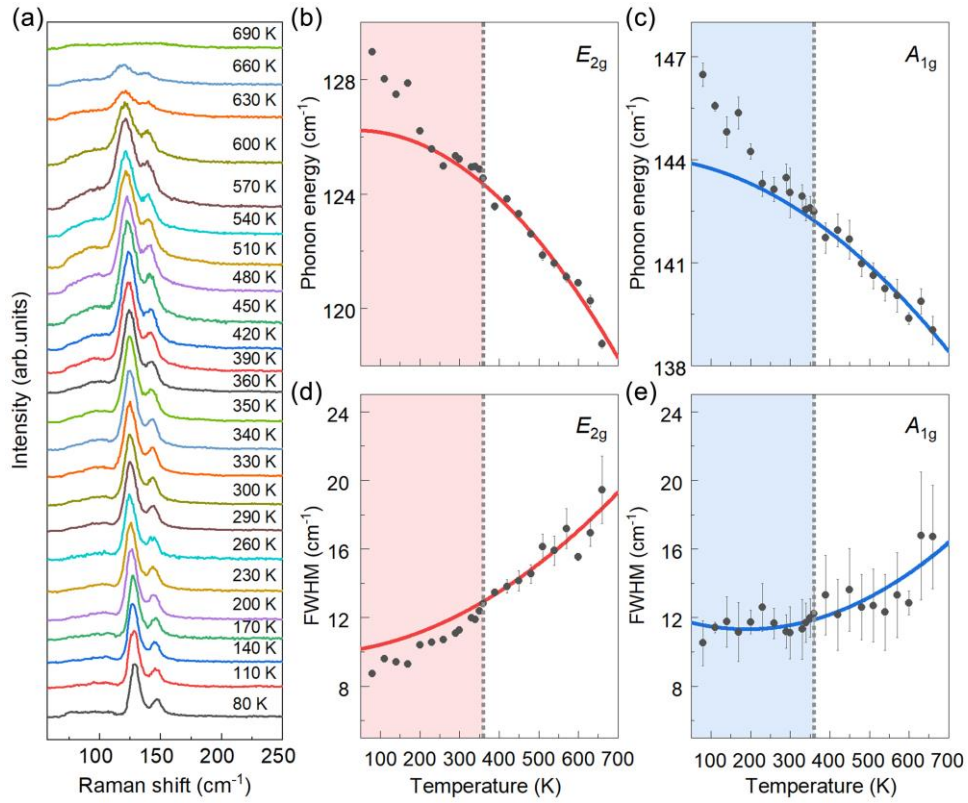


Fig. 4. (a) Raman spectroscopies of the Fe_3GaTe_2 at temperatures varying from 80 K to 690 K. Temperature-dependent phonon energies for the (b) E_{2g}^2 and (c) A_{1g}^1 modes. Temperature-dependent FWHMs for the (d) E_{2g}^2 and (e) A_{1g}^1 modes. The red and blue lines are fitted results using phonon anharmonic processes.

In conclusion, lattice dynamics and phonon dispersion of the vdW-layered Fe_3GaTe_2 have been thoroughly investigated using Raman spectroscopic measurements and first-principles calculation. Pressure- and temperature-dependent Raman spectroscopic measurements indicate that the vibrational mode of E_{2g}^2 at 126.0 cm^{-1} is anharmonic and that of A_{1g}^1 at

143.5 cm^{-1} is quasi-harmonic, and magnetic ordering plays a crucial role in lattice dynamics. The anomalous temperature dependency of phonon energy below the T_c of 360 K indicate the presence of spin-phonon coupling, underscoring the significant role of the lattice dynamics in Fe_3GaTe_2 ferromagnet. In summary, our findings provide a firm groundwork for the development of Fe_3GaTe_2 -based spin- and phonon-dependent microelectronic devices.

This work was supported by National Key Research and Development Program of China (MOST) (Grant No. 2022YFA1405100) and National Natural Science Foundation of China (NSFC)(Grant No. 52172272). The XPS test from Analytical and Testing Center in Sichuan University are acknowledged.

*Corresponding author.

gxiang@scu.edu.cn (G.X.)

Appendix A: Experimental section —The Fe_3GaTe_2 flakes were mechanically exfoliated and transferred onto SiO_2/Si substrate in glove box filled by high-purity N_2 (99.999%), and then sealed for physical measurements to avoid oxidization. The microstructures were investigated using HAADF-STEM measurement, where the Fe_3GaTe_2 sample was thinned using focused ion-beam milling technique (TESCAN LYRA3 FIB-SEM system). The compositional characterization was performed by X-ray photoelectron spectroscopy (XPS, Kratos AXIS Supra). The thickness was confirmed by atomic force microscopy (AFM, Bruker Dimension Icon). The magnetic properties were measured by superconducting quantum interference device (SQUID, Quantum Design MPMS). Raman spectra were detected in backscattering geometry using a solid-state excitation source of 532 nm (RGB Nova Pro, 300 mW; Laser spot, 5 μm). More information on self-assembled optical system for Raman measurement can be found in previous work [37]. For pressure-dependent Raman measurements, we loaded fresh Fe_3GaTe_2 flake into a rhenium-gasket diamond anvil cell (DAC) with 500 μm culets, and a mixture of methanol and ethanol with a stoichiometric ratio of 1:4 was used as pressure transmitting medium. Meanwhile, the pressure was calibrated by ruby fluorescence method with error within 0.5 GPa [38,39]. For temperature-dependent

measurements, the Fe₃GaTe₂ flake was loaded into a heating and freezing microscope stage (THMS600) ranging from 80-690 K.

Appendix B: Calculation section—The calculations were carried out utilizing Vienna *Ab initio* Simulation Package (VASP) [40,41], employing projector augmented wave (PAW) [42] pseudopotentials for electron-ion interactions and with the help of spin-polarized generalized gradient approximation (GGA) in the Perdew-Burke-Ernzerhof (PBE) form for exchange-correlation functional [43]. By DFT-D2 approach [44], the interlayer vdW interactions were considered. Initially, the crystal structural was fully releasing with energy cutoff of 450 eV for the plane waves. The Γ -centered $3\times 3\times 1$ k point meshes were set in Brillouin zone for bulk Fe₃GaTe₂, and total energy (force) convergence criteria was 10^{-8} eV (10^{-6} eV/Å). Subsequently, phonon calculations at $q=0$ were examined using density functional perturbation theory (DFPT) [45] in the VASP, followed by analysis with Phonopy software [46,47] to obtain the irreducible representation and corresponding frequencies across the entire Brillouin zone.

- [1] S. Q. Zhu and W. Zheng, *J. Phys. Chem. Lett.* **12**, 5216 (2021).
- [2] D. Zahn, F. Jakobe, Y. W. Windsor, H. Seiler, T. Vasileiadis, T. A. Butcher, Y. P. Qi, D. Engel, U. Atxitia, J. Vorberger, and R. Erbstorder, *Phys. Rev. Res.* **3**, 023032 (2021).
- [3] F. Metens, D. Mönkebücher, U. Parlak, C. Boix-Constant, S. Mañas-Valero, M. Matzer, R. Adhikari, A. Bonanni, E. Coronado, A. M. Kalashnikova, D. Bossini, and M. Cinchetti, *Adv. Mater.* **35**, 2208355 (2023).
- [4] X. Chen, X. Zhang, and G. Xiang, *Nanoscale*, **16**, 527 (2024).
- [5] G. Zhang, F. Guo, H. Wu, X. Wen, L. Yang, W. Jin, W. Zhang, and H. Chang, *Nat. Commun.* **13**, 5067 (2022).
- [6] A. M. Ruiz, D. L. Esteras, D. López-Alcalá, and J. Baldovi. *Nano Lett.* **24**, 7886 (2024).
- [7] J. E. Lee, S. Yan, S. Oh, J. Hwang, J. D. Denlinger, C. Hwang, H. Lei, S. K. Mo, S. Y. Park, and H Ryu, *Nano Lett.* **23**, 11526 (2023).
- [8] C. Zhang, Z. Jiang, J. Jiang, W. He, J. Zhang, F. Hu, S. Zhao, D. Yang, Y. Liu, Y. Peng, H. Yang, and H. Yang, *Nat. Commun.* **15**, 4472 (2024).
- [9] W. Li, W. Zhu, G. Zhang, H. Wu, S. Zhu, R. Li, E. Zhang, X. Zhang, Y. Deng, J. Zhang, L. Zhao, H. Chang, K. Wang, *Adv. Mater.* **35** 2303688 (2023).
- [10] G. Hu, H. Guo, S. Lv, L. Li, Y. Wang, Y. Han, L. Pan, Y. Xie, W. Yu, K. Zhu, Q. Qi, G.

- Xian, S. Zhu, J. Shi, L. Bao, X. Lin, W. Zhou, H. Yang, and H Gao, *Adv. Mater.* **36**, 2403154 (2024).
- [11] Z. Chen, Y. Yang, T. Ying, and J. Guo, *Nano Lett.* **24**, 993 (2024)
- [12] W. Jin, G. J. Zhang, H. Wu, L. Yang, W. F. Zhang, and H. X. Chang, *Nanoscale*, **15**, 5371 (2023).
- [13] X. Cong, X. L. Liu, M. L. Lin, and P. H. Tan, *npj 2D Mater. Appl.* **4**, 13 (2020).
- [14] O. Gomis, R. Vilaplana, F. J. Manjón, P. Rodríguez-Hernández, E. Pérez-González, A. Muñoz, V. Kucek, and C. Drasar, *Phys. Rev. B* **84**, 174305 (2011).
- [15] L. G. Pimenta Martins, R. Comin, M. J. S. Matos, M. S. C. Mazzoni, B. R. A. Neves, and M. Yankowitz, *Appl. Phys. Rev.* **10**, 011313 (2023).
- [16] Z. H. Yu, W. Xia, K. L. Xu, M. Xu, H. Y. Wang, X. Wang, N. Yu, Z. Q. Zou, J. G. Zhao, L. Wang, X. S. Miao, and Y. F. Guo, *J. Phys. Chem. C*, **123**, 13885 (2019).
- [17] N. T. Damh, D. P. Kozlenko, O. N. Lis, S. E. Kichanov, Y. V. Lukin, N. O. Golosova, B. N. Savenko, D. L. Duong, T. L. Phan, T. A. Tran, and M. H. Phan, *Adv. Sci.* **10**, 2206842 (2023).
- [18] Z. S. Lin, M. Lohmann, Z. A. Ali, C. Tang, J. X. Li, W. Y. Xing, J. N. Zhong, S. Jia, W. Han, S. Coh, W. Beyermann, and J. Shi, *Phys. Rev. Mater.* **2**, 051004(R) (2018).
- [19] T. Li, S. Jiang, N. Sivadas, Z. Wang, Y. Xu, D. Weber, J. E. Goldberger, K. Watanabe, T. Taniguchi, C. J. Fennie, K. F. Mak, and J. Shan, *Nat. Mater.* **18**, 1303 (2019).
- [20] Y. Y. Yin, X. L. Ma, D. Yan, C. J. Yi, B. B. Yue, J. H. Dai, L. Zhao, X. H. Yu, Y. Shi, J. T. Wang, and F. Hong, *Phys. Rev. B* **104**, 174114 (2021).
- [21] X. Q. Wang, Z. Y. Li, M. Zhang, T. Hou, J. G. Zhao, L. Li, A. Rahman, Z. L. Xu, J. B. Gong, Z. H. Chi, R. C. Dai, Z. P. Wang, Z. H. Qiao, and Z. M. Zhang, *Phys. Rev. B* **100**, 014407 (2019).
- [22] X. Chen, Q. Y. Luo, P. J. Guo, H. J. Zhou, Q. C. Hu, H. P. Wu, X. W. Shen, R. Y. Cui, L. Dong, T. X. Wei, Y. H. Xiao, D. R. Li, L. Lei, X. Zhang, J. F. Wang, G. Xiang, arXiv preprint arXiv:2406.02346, 2024.
- [23] G. J. Zhang, Q. Y. Luo, X. K. Wen, H. Wu, L. Yang, W. Jin, L. Li, J. Zhang, W. F. Zhang, H. B. Shu, H. X. Chang, *Chin. Phys. Lett.* **40**, 117501 (2023).
- [24] R. Loudon, *Adv. Phys.* **50**, 813 (2001).
- [25] L. Du, J. Tang, Y. Zhao, X. Li, R. Yang, X. Hu, X. Bai, X. Wang, K. Watanabe, T. Taniguchi, D. Shi, G. Yu, X. Bai, T. Hasan, G. Zhang, and Z. Sun, *Adv. Funct. Mater.* **29**, 1904734 (2019).
- [26] X. Kong, T. Berlijn, and L. Liang, *Adv. Electron. Mater.* **7**, 2001159 (2021).

- [27] K. Kamali, T. R. Ravindran, C. Ravi, Y. Sorb, N. Subramanian, and A. K. Arora, *Phys. Rev. B* **86**, 144301 (2012).
- [28] W. Ge, K. Xu, W. Xia, Z. Yu, H. Wang, X. Liu, J. Zhao, X. Wang, N. Yu, Z. Zou, Z. Yan, L. Wang, M. Xu, and Y. Guo, *J. Alloys Compd.* **819**, 153368 (2020).
- [29] Q. Cai, Y. Zhang, D. Luong, C. A. Tulk, B. P. T. Fokwa, and C. Li, *Adv. Phys. Res.* **2**, 2200089 (2023).
- [30] X. Gao, K. Zhai, H. X. Fu, J. Yan, D. Yue, F. Ke, Y. Zhao, C. Mu, A. Nie, J. Xiang, F. Wen, B. Wang, T. Xue, L. Wang, H. T. Yuan, and Z. Liu, *Adv. Sci.* **11**: 2402819 (2024).
- [31] Y. L. Su, J. J. Guo, X. R. Cheng, S. Q. Feng, and Y. J. Yang, *Alloys Compd.* **805**, 489 (2019).
- [32] J. M. Xu, S. Y. Wang, W. J. Wang, Y. H. Zhou, X. L. Chen, Z. R. Yang, and Z. Qu, *Chin. Phys. Lett.* **37**, 076202 (2020).
- [33] M. Balkanski, R. F. Wallis, and E. Haro, *Phys. Rev. B* 1983, **28**, 1928 (1983).
- [34] E. Granado, A. Garíca, J. A. Sanjurjo, C. Rettori, I. Torriani, *Phys. Rev. B* **60**, 11879 (1999).
- [35] A. Milosavljević, A. Šolajić, S. Djurdjić-Mijin, J. Pešić, B. Višić, Y. Liu, C. Petrovic, N. Lazarević, Z. V. Popović, *Phys. Rev. B* **99**, 214304 (2019).
- [36] M. Udagawa, K. Kohn, N. Koshizuka, T. Tsushima, and K. Tsushima, *Solid State Commun.* **16**, 779 (1975).
- [37] M. M. Zhao, B. B. Wu, J. Y. Liu, and L. Lei, *Chin. Phys. B* **32**, 090704 (2023).
- [38] H. K. Mao, J. Xu, and P. M. Bell, *J. Geophys. Res.: Solid Earth*, **91**, 4673 (1986).
- [39] C. M. Fan, S. Liu, J. Y. Liu, B. B. Wu, Q. Q. Tang, Y. Tao, M. F. Pu, F. Zhang, J. F. Li, X. L. Wang, D. W. He, C. Y. Zhou, and L. Lei, *Chin. Phys. Lett.* **39**, 026401 (2022).
- [40] G. Kresse, and J. Hafner, *Phys. Rev. B* **47**, 558 (1993).
- [41] G. Kresse, and J. Furthmuller, *VASP the GUIDE*, 2005.
- [42] P. E. Blochl, *Phys. Rev. B* **50**, 17953 (1994).
- [43] J. P. Perdew, K. Burke, M. Ernzerhof, *Phys. Rev. Lett.* **77**, 3865 (1996).
- [44] S. Grimme, *J. Comput. Chem.* **27**, 1787 (2006).
- [45] X. Gonze, and C. Lee, *Phys. Rev. B* **55**, 10355 (1997).
- [46] A. Togo, *J. Phys. Soc. Jpn.* **92**, 012001 (2023).
- [47] A. Togo, L. Chaput, T. Tadano, and I. Tanaka, *J. Phys.: Condens. Matter*, **35**, 353001 (2023).